Geochemistry, Geophysics, Geosystems

RESEARCH ARTICLE
10.1029/2020GC008925

Key Points:
- Images of upper mantle structure of southern Africa from body wave tomography show cratonic boundaries
- Anomalously fast lithosphere is imaged beneath the Etendeka Flood Basalt Province
- Images show little evidence for thermally driven plateau uplift of the Southern Africa Plateau

Supporting Information:
- Supporting Information S1
- Supporting Information S2

Correspondence to:
A. L. White-Gaynor,
alw361@psu.edu

Citation:
White-Gaynor, A. L., Nyblade, A. A., Durrheim, R., Raveloson, R., van der Meijde, M., Fadel, I., et al. (2020). Lithospheric boundaries and upper mantle structure beneath southern Africa imaged by *P* and *S* wave velocity models. *Geochemistry, Geophysics, Geosystems*, *21*, e2020GC008925. https://doi.org/10.1029/2020GC008925

Received 13 JAN 2020
Accepted 1 SEP 2020
Accepted article online 13 SEP 2020

Lithospheric Boundaries and Upper Mantle Structure Beneath Southern Africa Imaged by *P* and *S* Wave Velocity Models

A. L. White-Gaynor[1], A. A. Nyblade[1], R. Durrheim[2], R. Raveloson[2], M. van der Meijde[3], I. Fadel[3], H. Paulssen[4], M. Kwadiba[5], O. Ntibinyane[5], N. Titus[6], and M. Sitali[6]

[1]Department of Geosciences, The Pennsylvania State University, University Park, PA, USA, [2]School of Geosciences, The University of Witwatersrand, Johannesburg, South Africa, [3]Faculty of Geo-Information Science and Earth Observation (ITC), University of Twente, Enschede, Netherlands, [4]Department of Earth Sciences, Utrecht University, Utrecht, Netherlands, [5]Botswana Geosciences Institute, Lobatse, Botswana, [6]Geological Survey of Namibia, Windhoek, Namibia

Abstract We report new *P* and *S* wave velocity models of the upper mantle beneath southern Africa using data recorded on seismic stations spanning the entire subcontinent. Beneath most of the Damara Belt, including the Okavango Rift, our models show lower than average velocities (−0.8% Vp; −1.2% Vs) with an abrupt increase in velocities along the terrane's southern margin. We attribute the lower than average velocities to thinner lithosphere (~130 km thick) compared to thicker lithosphere (~200 km thick) immediately to the south under the Kalahari Craton. Beneath the Etendeka Flood Basalt Province, higher than average velocities (0.25% Vp; 0.75% Vs) indicate thicker and/or compositionally distinct lithosphere compared to other parts of the Damara Belt. In the Rehoboth Province, higher than average velocities (0.3% Vp; 0.5% Vs) suggest the presence of a microcraton, as do higher than average velocities (1.0% Vp; 1.5% Vs) under the Southern Irumide Belt. Lower than average velocities (−0.4% Vp; −0.7% Vs) beneath the Bushveld Complex and parts of the Mgondi and Okwa terranes are consistent with previous studies, which attributed them to compositionally modified lithosphere resulting from Precambrian magmatic events. There is little evidence for thermally modified upper mantle beneath any of these terranes which could provide a source of uplift for the Southern African Plateau. In contrast, beneath parts of the Irumide Belt in southern and central Zambia and the Mozambique Belt in central Mozambique, deep-seated low velocity anomalies (−0.7% Vp; −0.8% Vs) can be attributed to upper mantle extensions of the African superplume structure.

1. Introduction

Many studies of the tectonic framework of southern Africa, extending back more than 50 years, have strongly influenced our knowledge of Earth history and continental evolution (e.g., Anhaeusser, 1973; Brock, 1959; Kröner, 1977). However, the upper mantle structure in much of southern Africa remains poorly imaged, especially beneath Proterozoic mobile belts, limiting our understanding of African lithospheric evolution and the location of terrane boundaries at subcrustal depths. To date, there have been few seismological studies of southern Africa using data from seismic networks deployed in Proterozoic terranes surrounding the Archean blocks forming form the core of the Southern African Shield.

Data from recent deployments of broadband seismic stations in regions peripheral to the greater Kalahari Craton provide an opportunity to image the upper mantle beneath southern Africa more broadly than possible previously (Figure 1). In this investigation, we utilized data from several newer seismic networks, along with data from older networks, to develop *P* and *S* wave velocity models of the upper mantle covering most of southern Africa. Our models reveal structure beneath areas of southern Africa not previously imaged by regional body wave tomography studies, and also provide improved resolution of structure beneath previously studied regions.

In the interpretation of our models, we not only reexamine the Precambrian tectonic framework of southern Africa, but also investigate if there is evidence for thermally perturbed upper mantle beneath southern Africa, particularly beneath the uplifted regions of the Southern African Plateau. There has been much discussion (e.g., Adams & Nyblade, 2011; Li & Burke, 2006; Nyblade & Sleep, 2003; and references therein)

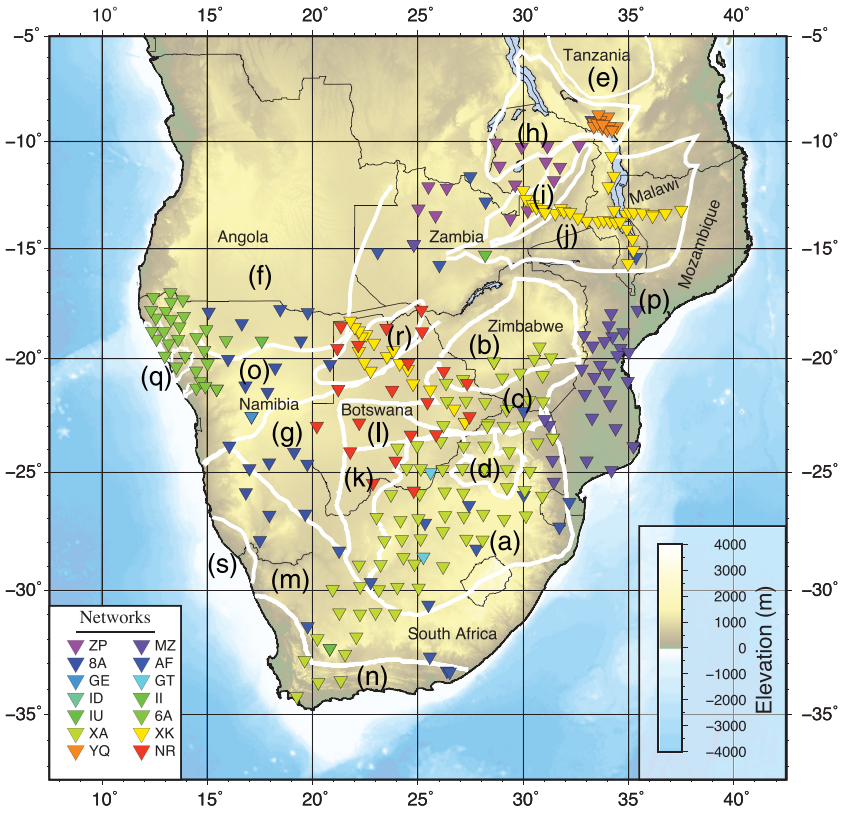

Figure 1. Topographic map showing tectonic boundaries in southern Africa and locations of seismic stations used in the *P* wave and *S* wave models. Tectonic terranes are labeled as (a) Kaapvaal Craton; (b) Zimbabwe Craton; (c) Limpopo Belt; (d) Bushveld Igneous Province; (e) Tanzania Craton; (f) Congo Craton/Angolan Shield; (g) Rehoboth Province; (h) Bangweulu Block; (i) Irumide Belt; (j) Southern Irumide Belt; (k) Kheis Belt; (l) Okwa Terrane; (m) Namaqua-Natal Belt; (n) Cape Fold Belt; (o) Damara Belt; (p) Mozambique Belt; (q) Etendeka Flood Basalt Province; (r) Okavango Rift; (s) Gariep Belt (Begg et al., 2009; Frimmel & Frank, 1998). Elevations from GEBCO (Weatherall et al., 2015).

about the thermal state of the upper mantle beneath southern Africa and the extent to which upper mantle thermal anomalies provide buoyant support for the ~1-km-high Southern African Plateau (Nyblade & Robinson, 1994) (Figure 1). Because of limited seismic data coverage in many regions of southern Africa prior to this study, and in particular in Proterozoic terranes, the origin of high elevation across southern Africa remains unresolved. In comparison, to the north in eastern Africa, thermally perturbed upper mantle, revealed by seismic images, clearly provides sufficient buoyant support to account for the ~1-km-high East African Plateau (e.g., Adams et al., 2012; Bagley & Nyblade, 2013; Hansen et al., 2012; Mulibo & Nyblade, 2013a, 2013b). The results of this study enable us to comment on whether the upper mantle beneath the study area has been thermally perturbed, thus providing a possible source of buoyancy (i.e., uplift) for the Southern African Plateau.

2. Tectonic Background

The tectonic framework of the Southern African Shield can be divided into three parts (Figure 1). (1) The ancient core of the shield consists of several Archean cratons. (2) The cratons are surrounded and welded together by mobile belts accreted and deformed during major orogenic cycles during the Phanerozoic. (3) A number of the Precambrian terrains have experienced Phanerozoic compressional tectonics, rifting, and flood basalt volcanism. The most recent phase of rifting within southern Africa extends south and southwest from the Cenozoic East African Rift System (EARS).

There are three main Archean blocks within the study area. The Kaapvaal and Zimbabwe cratons are both granite-greenstone terranes that formed in the Mesoarchean to Neoarchean (de Wit et al., 1992; Figure 1).

The Limpopo Belt is a Neoarchean deformational belt that formed during the collision of the Kaapvaal and Zimbabwe cratons. Combined, these terranes are commonly referred to as the greater Kalahari Craton (de Wit et al., 1992). The last major tectonothermal events to affect these terranes were the emplacement of the Great Dike in the Zimbabwe Craton c. 2.6 Ga (Jelsma & Dirks, 2002) and formation of the layered Bushveld igneous complex (Figure 1) within the Kaapvaal Craton c. 2.1 Ga (Olsson et al., 2010) (Figure 1). Extending from southern Angola northward to Cameroon is the expansive Congo Craton and Angolan Shield, a complex amalgamation of Archean and Proterozoic crustal blocks, much of which is covered by Phanerozoic sediments (Batumike et al., 2009).

The Proterozoic history of southern Africa is marked by continental growth through the accretion of younger terranes to the Archean blocks (Figure 1). During the Paleoproterozoic, the Kheis Belt and Rehoboth Province accreted to the western margin of the Kaapvaal Craton (Hanson, 2003). This was followed by the formation of the Namaqua-Natal Mobile Belt surrounding the southern margin of the Kaapvaal Craton and Rehoboth Province c. 1.2–1.0 Ga (Cornell et al., 2011). To the northwest, the Magondi and Okwa terranes accreted to the Kahalari Craton c. 2.0 Ga (McCourt et al., 2001). In the northernmost portion of the study area, the Irumide and Southern Irumide Belts formed in the Mesoproterozoic c. 1.3–1.0 Ga; however, some evidence suggests that these belts were extensively reworked during the Neoproterozoic Pan-African orogeny (Hanson, 2003).

There are two major Pan-African orogenic belts within the study area. In the eastern portion of the study area, the Mozambique Belt formed during the final assembly of Gondwana c. 841–632 Ma (Hanson, 2003). In the northwest, the Damara-Ghanzi-Chobe Belt (hereafter referred to as the Damara Belt) formed during the collision of the greater Kalahari Craton and the Congo Craton c. 580–500 Ma. During roughly the same time, small portions of the western margin of the Namaqua-Natal Belt were overprinted with the accretion of the Gariep Belt in southern Namibia (Eglington, 2006).

Several tectonic events punctuate the Phanerozoic history of southern Africa. The c. 250 Ma Cape Fold Belt, the youngest collisional belt in the study region, is located along the southern tip of the African continent and resulted from subduction and arc deformation at or near the southern margin of Gondwana (Begg et al., 2009; Hansma et al., 2016). The initial breakup of Gondwana coincided with Karoo rifting across southern Africa and the formation of the c. 180 Ma Karoo large igneous province (Duncan et al., 1997). The c. 130 Ma Etendeka large igneous province in northwestern Namibia is also associated with the breakup of Gondwana, as well as the Tristan Da Cunha mantle plume (Bauer et al., 2000). The Cenozoic Era is marked by the formation of incipient rifts resulting from the southward extension of the EARS. Seismically active fault systems point to incipient rifting within the Okavango Rift Zone (ORZ) in northern Botswana (Scholz et al., 1976), and also define the southernmost extension of the Western Branch of the EARS in central Mozambique (Fonseca et al., 2014).

The topography of southern Africa is characterized by a ~1-km-high plateau (Figure 1), which together with the East African Plateau and the southeastern Atlantic Basin comprise the African Superswell (Nyblade & Robinson, 1994). The buoyancy support for and the timing and rate of uplift of the Southern African Plateau is not well understood (Nyblade & Sleep, 2003, and references therein). Several mechanisms have been proposed for the buoyancy support of the region, including density anomalies and flow associated with the African Superplume in the middle-to-lower mantle (Forte et al., 2010; Gurnis et al., 2000; Lithgow-Bertelloni & Silver, 1998) and thermally perturbed upper mantle beneath the Kalahari Craton (Li & Burke, 2006). Recently, noble gas compositions with a lower mantle signatures have been recorded in CO_2 seeps in southeastern Africa, suggesting the presence of a mantle plume beneath the region (Gilfillan et al., 2019).

3. Previous Geophysical Studies

The crustal structure of southern Africa has been extensively examined using a range of seismological observations and models. Crustal thickness in the Kalahari Craton, and more recently portions of the surrounding Proterozoic terranes, has been characterized by receiver function analysis (Fadel et al., 2018; James et al., 2001; Nair et al., 2006; Nguuri et al., 2001; Yu et al., 2015), through joint inversion of receiver functions and surface wave dispersion measurements (Kachingwe et al., 2015; Kgaswane et al., 2009); by modeling regional seismic phases (Kwadiba et al., 2003; Wright et al., 2003); and by inverting satellite gravity data

(Tugume et al., 2013). Consistent across all of these studies is a range of crustal thicknesses of ~34–50 km within the cratonic blocks and surrounding mobile belts.

There have been several previous body wave tomography investigations in southern Africa, all capitalizing on expanding data coverage in the region. The earliest models were constructed using data from the Southern African Seismic Experiment (SASE) within the Kalahari Craton (Figure 1). Fouch et al. (2004) modeled ±2% *P* wave and ±2.4% *S* wave velocity variations within the Kalahari Craton, Namaqua-Natal Belt, and Cape Fold Belt. High velocity anomalies demarcating the cratonic region were present to depths of ≥300 km, while a low velocity anomaly was imaged beneath the Bushveld Complex. More recently, finite-frequency tomography has been applied to the SASE data set, yielding similar results (Youssof et al., 2015). Yu et al. (2015), using data from the Seismic Arrays for African Rift Initiation (SAFARI) network in Botswana, published one of the first regional-scale body wave tomography studies on structure outside of the Kalahari Craton. They reported models showing a low velocity (−1–2% Vp) anomaly beneath the ORZ in northern Botswana, extending to a depth of ≤300 km.

Expanding on these previous studies, Ortiz et al. (2019) incorporated data from the SASE and SAFARI data sets with data from the Botswana Network of Autonomously Recording Seismographs project and AfricaArray seismic stations in Zambia to develop *P* wave and *S* wave velocity models for a broader region of southern Africa. While their models show a similar degree of variability in seismic velocities to previous models within the Kalahari Craton, Namaqua-Natal Belt, Cape Fold Belt, and the ORZ, they also imaged lower velocities beneath the Damara Belt in northern Botswana away from the ORZ and a rapid transition to higher velocities along the terrane's southern margin. They interpreted this transition as the northern edge of the greater Kalahari Craton. The Ortiz et al. (2019) model also shows a continuation of the low velocity anomaly beneath the Bushveld Complex to the northwest into central Botswana.

Further to the north in southern Zambia, the Ortiz et al. (2019) model shows a deep-seated low velocity anomaly extending at least as deep as the mantle transition zone. This feature was first reported by Mulibo and Nyblade (2013a, 2013b), who argued that the anomaly extends across the transition zone connecting the low velocity structure in the lower mantle beneath southern Africa, which has been often referred to as the African Superplume, with thermally perturbed upper mantle beneath eastern Africa. Because the Ortiz et al. (2019) model only imaged upper mantle structure beneath the portion of the Damara Belt in northern Botswana and southern Zambia, Ortiz et al. were not able to determine if the low velocity anomaly under the Damara Belt in northern Botswana, including the ORZ, extended to the southwest beneath the Damara Belt in northern Namibia.

Complementing the body wave models are many surface wave investigations of the upper mantle beneath southern Africa. Continental-scale velocity models have been developed by inverting fundamental and/or higher mode Rayleigh and Love wave measurements (e.g., Chevrot & Zhao, 2007; Fishwick, 2010; Pasyanos & Nyblade, 2007; Priestley et al., 2008; Raveloson et al., 2015; Ritsema & van Heijst, 2000; Sebai et al., 2006) and modeling the ambient noise wavefield (Emry et al., 2019). A number of regional-scale models have been published using the two-plane wave approximation of teleseismic Rayleigh waves (Forsyth & Li, 2005) for southern (Adams & Nyblade, 2011; Li & Burke, 2006; Li & Li, 2015) and eastern (Adams et al., 2012; O'Donnell et al., 2013; Weeraratne et al., 2003) Africa. Helmholtz tomography using interstation measurements of Rayleigh wave phase velocities has yielded comparable results in eastern Africa to the two-plane wave models (Accardo et al., 2018; Adams et al., 2018). Consistent across these models is the presence of a higher velocity upper mantle lid underlying cratonic portions of the subcontinent and lower shear velocity structure in the upper mantle beneath the mobile belts, with the most pronounced low velocity anomalies beneath the rifted mobile belts in eastern Africa.

Magnetotelluric methods also have been used to image upper mantle structure beneath southern Africa and parts of eastern Africa. Khoza et al. (2013) imaged thinner lithosphere beneath the Damara Belt (~180 km) than beneath the Kalahari and Congo cratons (~250 km). Consistent with the Khoza et al. (2013) study, Muller et al. (2009) reported ~160-km-thick lithosphere beneath the Damara Belt, and Miensopust et al. (2011) reported ~180-km-thick lithosphere beneath the ORZ. Within the Rehoboth Province, Muller et al. (2009) also imaged ~180-km-thick lithosphere. To the north, in eastern Zambia and southern Malawi, Sarafian et al. (2018) reported a deep resistive lithospheric root (~250 km) beneath the Southern Irumide Belt, which they interpreted as a remnant of the pre-Mesoproterozoic Niassa Craton.

4. Data and Methods

Figure 1 shows the location of seismic stations used in this study. This investigation was motivated by new data from the 2015–2018 deployment of 19 AfricaArray broadband seismic stations in Namibia (10.7914/SN/8A_2015). To complement those data, and to provide a check on consistency with previous studies, we used data from an additional 13 temporary and permanent networks in southern Africa covering a timespan from 1997–2018. In Namibia, we included data from 28 stations deployed from 2010–2012 as part of the Walpass network (10.14470/1N134371), and contemporaneous with both the AfricaArray-Namibia and Walpass networks, data from a single station from the GEOFON network in Windhoek (10.14470/TR560404). In Botswana, data from 38 stations were used, including 17 stations from the SAFARI network (10.7914/SN/XK_2012) and 21 stations from the Botswana Network of Autonomously Recording Seismographs (10.7914/SN/NR). In the northern portion of our study area, we used data from 33 stations deployed as part of the SAFARI project, 23 stations from the AfricaArray Uganda/Tanzania/Zambia network (10.7914/SN/ZP_2007), 14 stations from the Study of Extension and Magmatism in Malawi and Tanzania (SEGMeNT) project (10.7914/SN/YQ_2013), along with data from a few permanent stations (10.7914/SN/II, 10.7914/SN/IU, 10.7914/SN/GT, 10.7914/SN/ID). In Mozambique, we used data from 24 stations in the Mozambique Rift Tomography (MOZART) project, and in Zimbabwe, Botswana, and South Africa, data from 75 stations in the SASE network (10.7914/SN/XA_1997) together with data from five permanent stations (http://www.fdsn.org/networks/detail/IU; 10.7914/SN/II; 10.7914/SN/GT; https://geofon.gfz-potsdam.de/doi/network/GE; and https://doi.org/10.7914/SN/ID). In total, data from 278 stations were used for the *P* wave model and from 273 stations for the *S* wave model (supporting information Table S1).

From these data, we obtained *P* and *S* relative arrival times from M > 5.5 teleseismic earthquakes at epicentral distances ranging from 30–90° for *P* waves and 30–84° for *S* waves. Waveforms were first corrected for instrument response and then filtered between 0.5 and 5 Hz for *P* waves and 0.04 and 2 Hz for *S* waves. *P* and *S* wave arrivals were hand-picked on a prominent phase before applying a multichannel cross-correlation approach of VanDecar and Crosson (1990) to measure more precise relative arrival times for events with three or more manual picks. This technique uses a 3-s window for *P* waves and a 12-s window for *S* waves around the initial picks, and cross-correlates all combinations of traces for each event to find the ensemble correlation maxima. Events with cross-correlations values >0.70 for all combinations of windowed traces were used, resulting in a total of 693 useful events for *P* waves and 493 events for *S* waves (Figure S1, Table S2). These events yielded 13,326 unique *P* wave and 9,242 unique *S* wave relative arrival-time measurements. Although there is some overlap in the data used in this study and by Ortiz et al. (2019), all of the data used by Ortiz et al. (2019) were re-cross-correlated with data from stations spread more broadly across the study region for obtaining relative arrival times.

The model domain consists of a series of intersecting knots spaced relative to lines of latitude and longitude, and in kilometers with depth. The model ranges from 37.5°S to 7.5°S with knots spaced at 0.5° increments, and from 8.0°E to 41°E with knots also at 0.5° intervals. Knots were spaced at 20 km intervals between the surface and 200 km depth, at 33 km intervals between 200 and 700 km depth, at 50 km intervals from 700–1,400 km depth, and at 100 km intervals from 1,400–1,600 km depth. In total, the model includes 59 knots in latitude, 65 knots in longitude, and 42 knots in depth.

To solve for a 3-D velocity model, we first numerically calculated partial derivatives at each knot with respect to slowness using perturbations from the 1D IASP91 model (Kennett & Engdahl, 1991). Initial travel-time residuals were calculated by ray tracing event-receiver paths through the 1-D model. During the inversion process, we iteratively update the 3-D model using a conjugate-gradient approach through reducing the travel-time residuals until changes in the model made insignificant (<0.01 s) changes to the RMS travel-time residual (VanDecar, 1991). The inversion simultaneously solves for 3-D changes to the velocity model, station static terms, and event relocation terms. Station static terms account for structure in the shallowest part of the model where there is limited ray crossing, while the event relocation terms absorb location error and structure outside of the model domain. To avoid overfitting the data, the system of equations was regularized by the Huber norm. Coefficients were downweighed by the L2 norm for residuals from the previous iteration within 1.5 standard deviations from the mean and by the L1 norm for residuals greater than 1.5 standard deviations of the mean, as the L1 norm more aggressively downweighs the coefficients. Weights for the smoothing (flattening) and damping terms were chosen using a tradeoff curve, providing 96.7% rms

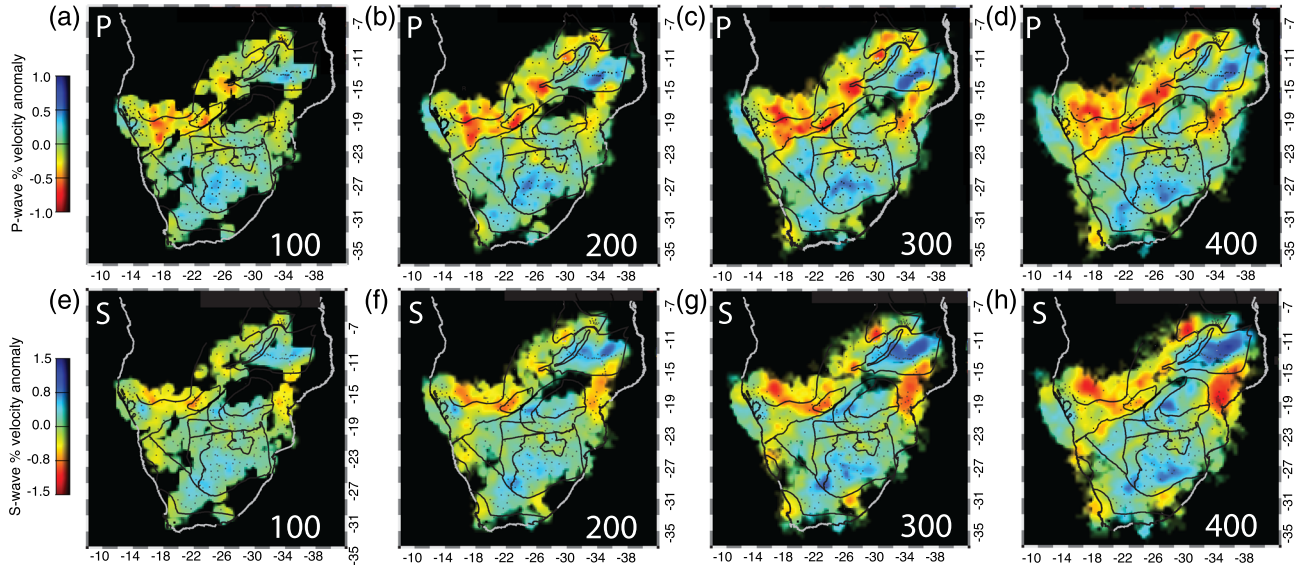

Figure 2. Horizontal cross-sections through the *P* wave (a–d) and *S* wave (e–h) models at 100 km increments. Depth (km) below the surface is labeled in white text. Tectonic boundaries correspond to those in Figure 1.

travel-time residual reduction in the *P* wave model and 86.5% travel-time residual reduction in the *S* wave model (Figure S2). The large reduction in the rms travel-time residual is a product of the contributions from the event relocation terms (median = 7.3 s), the station static terms (Figure S8), and the model velocity perturbations (Figure 2).

5. Model Results

Horizontal slices through the model are shown in Figure 2, and vertical slices in Figures 3 and 4. Velocity structure in the top 50 km of the models is not shown because ray crossing is limited at these depths. The mean of the model could have shifted from the starting model during the inversion process and so absolute velocities are unconstrained. To first-order, the *P* wave and *S* wave models are similar and anomalies in both models are well correlated with terranes shown in Figure 1. In the following paragraphs, we summarize the velocity structure in both models.

The Kaapvaal Craton is the largest high velocity anomaly (Anomaly A, Figures 3a and 3f) in the models. In the upper 600 km, the average *P* wave velocity in this region is ~ + 0.5%, with a maximum of +0.8% at 300 km depth. The *S* wave velocity is also higher than average across the Kaapvaal Craton in the upper 600 km, with a peak anomalous velocity of +1.0% at 400 km depth. There is, however, a region in the upper 400–500 km within the northern Kaapvaal Craton with lower than average Vp (−0.4%) and Vs (−0.7%) (Anomaly B, Figures 3a, 3f, and 3g) that correlates with the Bushveld Igneous Complex and extends to the northwest into central Botswana. The Zimbabwe Craton has higher than average velocity (Vp and Vs) in the west and lower than average velocities in the east bordering the Mozambique Belt.

In the southern part of the model, both the *P* and *S* wave velocities are lower than average beneath the Cape Fold Belt. North of that, beneath the Namaqua-Natal Belt, the velocities are near average in the top 300 km, except in a region directly south of the Kheis Belt, where both the *P* wave and *S* wave velocities are higher than average between 300 and 500 km depth. Within the Kheis Belt, the *P* wave and *S* wave models have average velocity structure. To the west of the Kheis Belt, there is strong similarity between the *P* wave and *S* wave models beneath the Rehoboth Province, with an increasing trend in velocities in the upper 400 km from −0.25% Vp and −0.5% Vs in the west to +0.3 to +0.4% Vp and +0.5% Vs in the east.

Within the Damara Belt, a low velocity anomaly is present throughout most of the upper mantle (Anomalies C, D, and F, Figures 3a, 3b, and 3d). There is a consistent −0.3% to −0.75% Vp and −0.5 to −0.8% Vs anomaly in the upper ~400 km of the model, with the lowest velocities (−0.75% Vp and −0.9% Vs) at ~250 km depth.

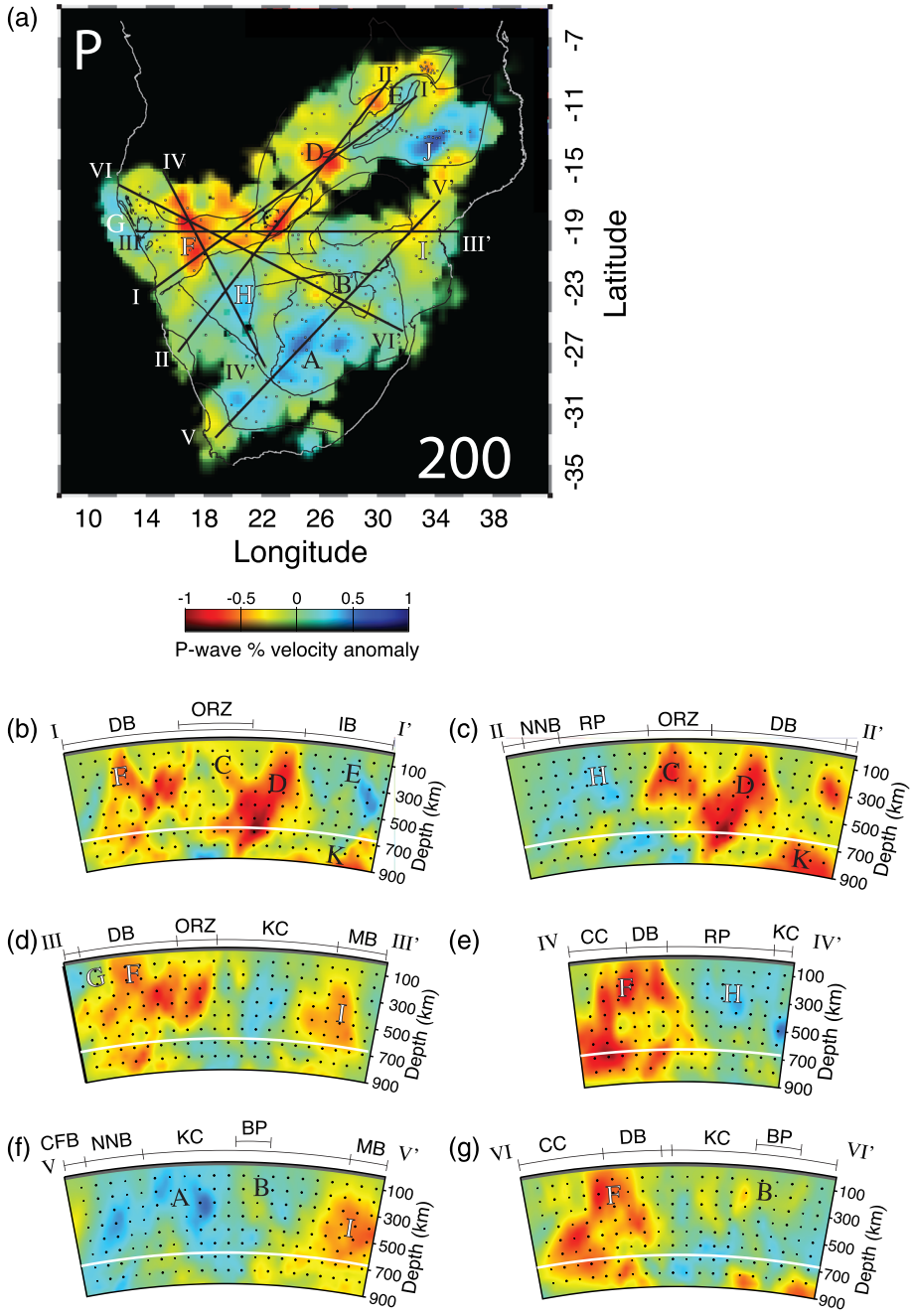

Figure 3. (a) Horizontal cross-section through the *P* wave model at 200 km depth. Major velocity anomalies are labeled A–K, where black text represents anomalies discussed in previous work and white text represents newly imaged anomalies. Locations of cross-sections I–VI in panels (b)–(g) are shown with black line segments. Tectonic boundaries are the same as those in Figure 1. (b–g) Vertical cross-sections taken through the *P* wave model. BP = Bushveld Province; DB = Damara Belt; CC = Congo Craton; CFB = Cape Fold Belt; IB = Irumide Belt; KC = Kaapvaal Craton; MB = Mozambique Belt; NNB = Namaqua-Natal Belt; ORZ = Okavango Rift Zone; RP = Rehoboth Province.

The low velocity anomaly extends northward beneath southern Angola at depths greater than 400 km. There is a strong spatial correlation between the southern edge of the LVZ and the boundary between the Damara Belt and Rehoboth Province (Figure 2).

Within the ORZ, both the *P* wave and *S* wave models have lower than average velocities (−1.0%, Anomaly C, Figure 3b) in the upper 400 km. This structure is separated by a region of higher velocities from the LVZ

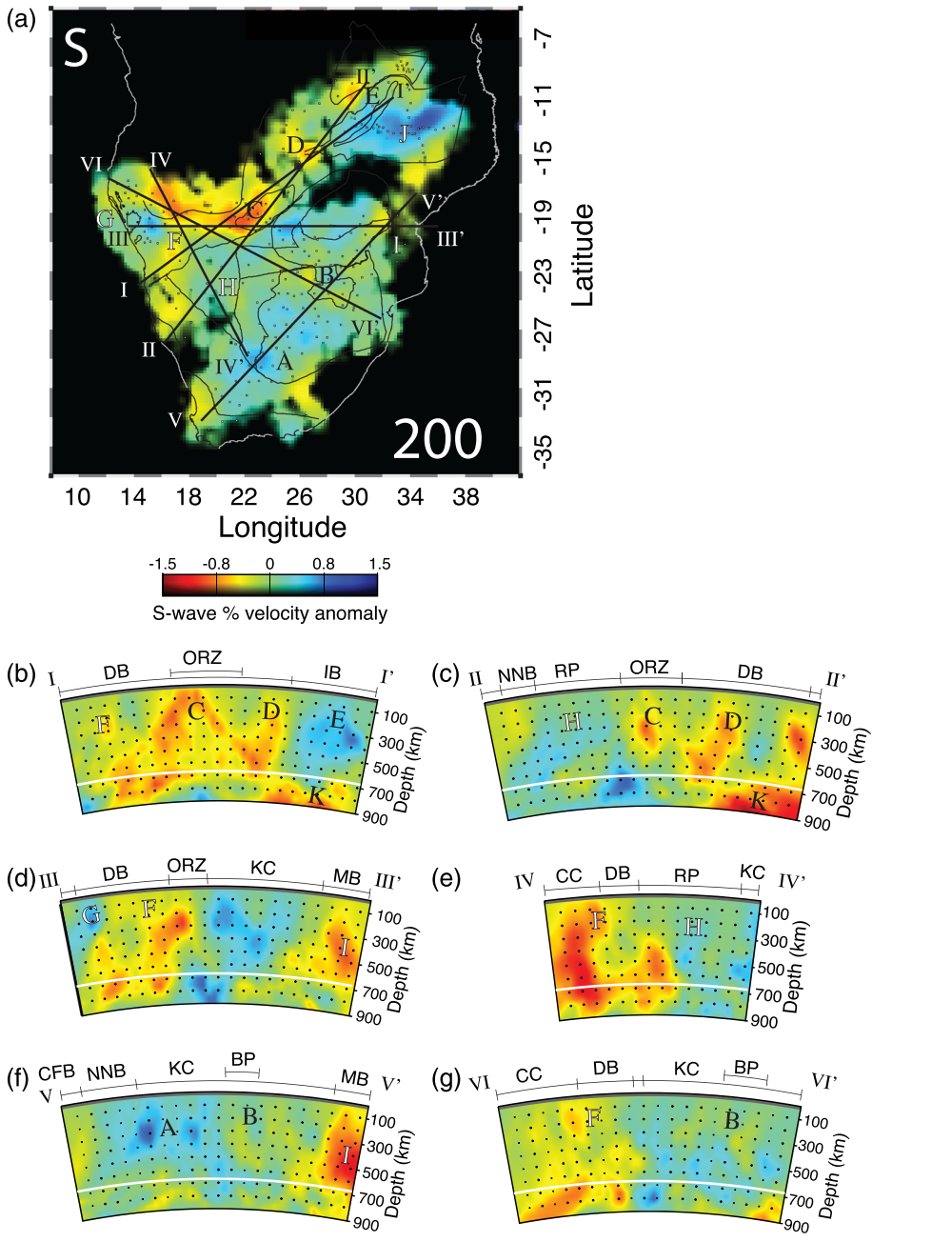

Figure 4. (a) Horizontal cross-section through the *S* wave model at 200 km depth. Major velocity anomalies are labeled A–K, where black text represents anomalies discussed in previous work and white text represents newly imaged anomalies. Locations of cross-sections I–VI in panels (b)–(g) are shown with black line segments. Tectonic boundaries are the same as those in Figure 1. (b–g) Vertical cross-sections taken through the *S* wave model. Intersected anomalies (A–J) are labeled. BP = Bushveld Province; DB = Damara Belt; CC = Congo Craton; CFB = Cape Fold Belt; IB = Irumide Belt; KC = Kaapvaal Craton; MB = Mozambique Belt; NNB = Namaqua-Natal Belt; ORZ = Okavango Rift Zone; RP = Rehoboth Province.

extending to the NW from the Bushveld Complex into central Botswana. Unlike the majority of the Damara Belt, beneath the Etendeka Flood Basalt Province in northwestern Namibia, *P* wave velocities are +0.25% in the top 200 km of the mantle (Anomaly G, Figures 3a and 3d).

Beneath the Damara Belt in southcentral Zambia, the *P* wave model has a low velocity anomaly extending to a depth of ≥800 km (Anomaly D, Figures 3a and 3b), with maximum negative velocities of −0.9% between

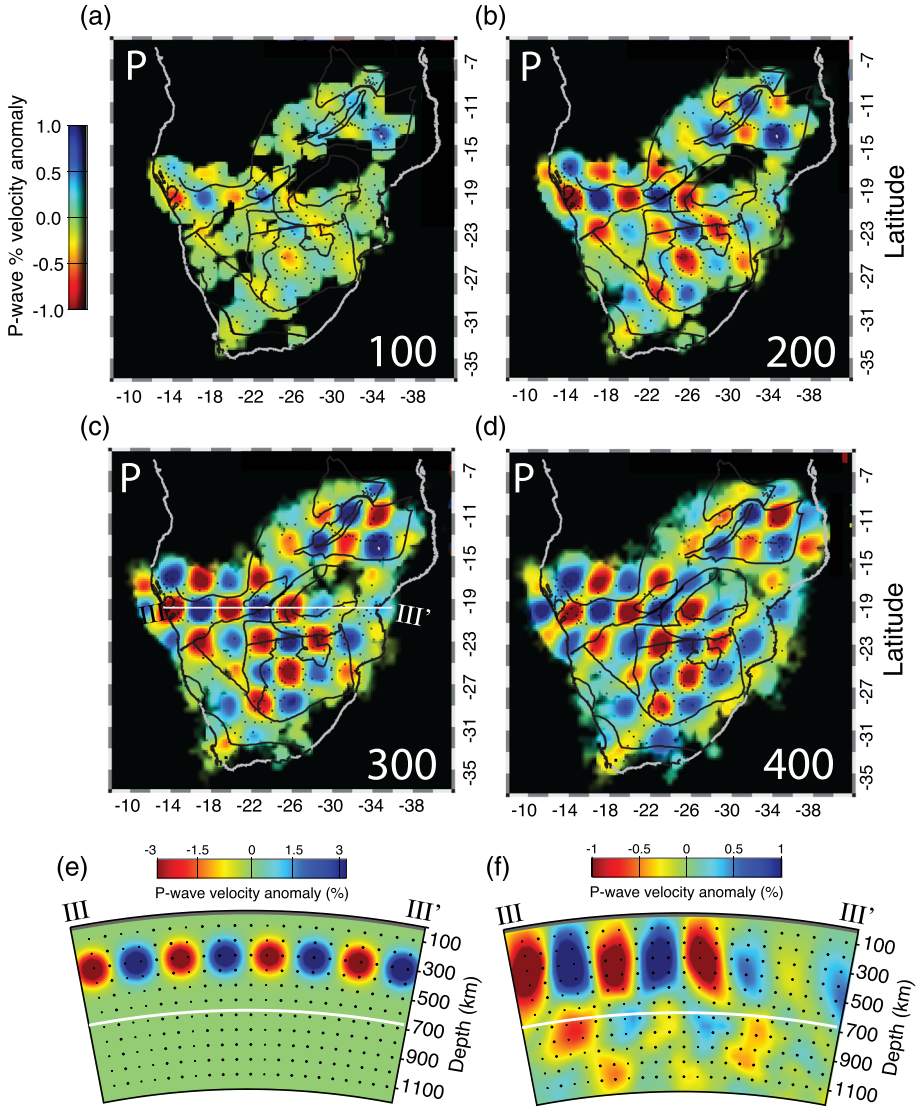

Figure 5. (a–d) Horizontal cross-sections of *P* wave checkerboard resolution tests taken at 100-km intervals (100–400 km). White line in (c) shows location of vertical cross-section III–III′ in (e) and (f). (e) Synthetic *P* wave velocity model used to create an artificial travel-time data set. Inversion results from this synthetic data set are shown in (c) and (f).

600 and 800 km depth. This feature is also present in the *S* wave model, but slightly weaker with a peak negative anomaly of −0.7%. The deepest structure present in both the *P* wave and *S* wave models is a large low velocity anomaly at ≥700 km depth (Anomaly K) centered beneath the Irumide Belt in northern Zambia with peak Vp of −0.5% and Vs of −1.5% Vs.

In the upper mantle between 200 and 450 km depth, at the edge of resolution in the models, the western side of the Bangweulu Block is characterized by lower than average velocities. There is a high velocity anomaly (Anomaly E, Figures 3a and 3b) in the upper 400 km along the eastern side of the Bangweulu Block and beneath the Irumide Belt. Within the Malawi Rift, beneath the northern edge of Lake Malawi, a focused negative velocity anomaly (−0.5% Vp and −0.25% Vs) is present in the upper 300 km. Within the Southern Irumide Belt, the *P* wave model has a high velocity anomaly with peak velocities of +1.0% between depths of 400 and 500 km (Anomaly J, Figure 3a). In the *S* wave model, Anomaly J and Anomaly E merge together to form a broad high velocity anomaly covering a wide portion of the Irumide Belt and Southern Irumide Belt. South of the Irumide Belt, beneath the Mozambique Belt in central Mozambique, both models

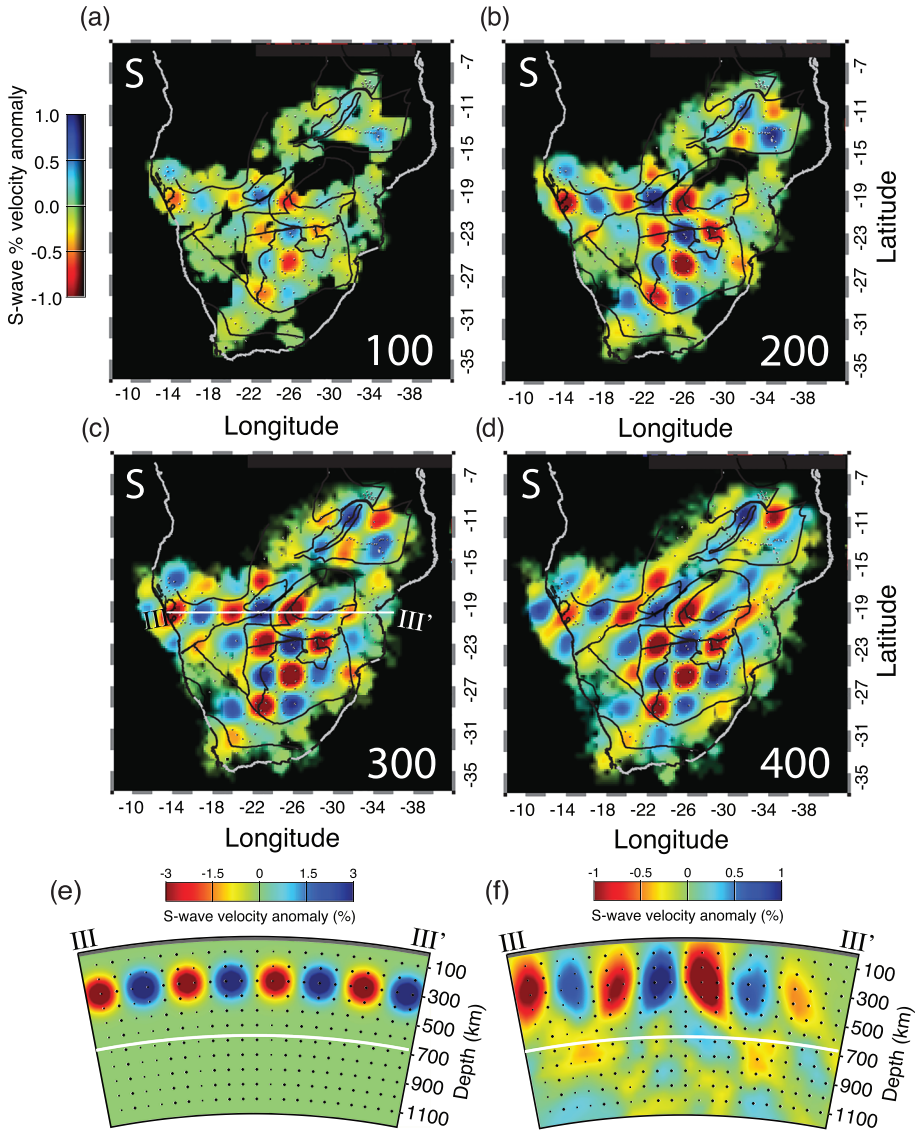

Figure 6. (a–d) Horizontal cross-sections of *S* wave checkerboard resolution tests taken at 100-km intervals (100–400 km). White line in (c) shows location of vertical cross-section III-III′ in (e) and (f). (e) Synthetic *S* wave velocity model used to create an artificial travel-time data set. Inversion results from this synthetic data set are shown in (c) and (f).

have a low velocity anomaly (Anomaly I, Figure 3a) that extends to ≥700 km depth. The *P* wave model has a peak anomalous velocity of −0.7% and the *S* wave model has a peak anomalous velocity of −0.8%. In southern Mozambique, both the *P* and *S* wave models have <0.3% variation from average.

6. Model Resolution

For assessing the vertical and horizontal resolution of our *P* and *S* wave velocity models, we inverted a series of synthetic data sets to check for recoverability. To evaluate the spatial resolution of the model at various depth ranges, we raytraced our event and station geometry through checkerboard models to create synthetic travel-time data sets. A normal distribution of noise was added to the synthetic travel-times, centered at the origin with a standard deviation of 0.04 s for the *P* waves and 0.10 s for the *S* waves. Checkerboard models were designed with alternating high and low anomalies. The spherical anomalies had a Gaussian shape, with a maximum anomalous amplitude of ±5% and a half-maximum width of 200 km. The centers of the

Table 1
Summary of Anomalies in P and S Wave Models

Anomaly	Interpretation
A	Thicker cratonic lithosphere of the Kalahari Craton
B	Modified cratonic lithosphere beneath the Bushveld Igneous Complex
C	Possibly thinned lithosphere under the Okavango Rift Zone
D	Upper mantle expression of the African Superplume
E	Thicker cratonic lithosphere within the Bangweulu Block
F	Thinner off-craton lithosphere beneath the Damara Belt
G	Depleted lithospheric root beneath the Etendeka Flood Basalt Province
H	Thicker cratonic lithosphere within the Rehoboth Province
I	Upper mantle expression of the African Superplume beneath southern EARS
J	Thicker cratonic lithosphere beneath the Niassa Craton
K	Lower mantle expression of the African Superplume

anomalies were spaced 3° apart in both latitude and longitude. The results of the checkerboard inversion are shown in Figures 5 and 6. Regions with the recovered pattern are considered areas in which the model is able to resolve structures 200–300 km-wide or wider. Only larger-scale features are considered interpretable in regions where the pattern is not recovered. Below 600 km depth, we increased the half-maximum width of the anomalies to 400 km to test for recoverability of structures between 400 and 600 km in diameter or greater (Figures S5 and S6).

Regions of high recoverability are in areas with denser station coverage. While recovery of input structures centered at 100 km depth is limited in most regions, at deeper depths the checkerboard pattern is better resolved, particularly at depths ≥200 km. From 200–600 km depths, the *P* wave model has good recoverability of the ~200-km-wide input anomalies in most regions with the exception of northern Zimbabwe, Mozambique, and the southern coast of South Africa. Recovery of the larger checkerboards at ≥700 km depth is largely ubiquitous, with some northeast-southwest smearing. Vertical smearing, common in body wave tomography, is evident, with checkerboard structures stretching ~150 km upward and downward (Figures 5e–5f and 6e–6f).

Overall, the pattern of recovery in the *S* wave model is similar to the *P* wave model, with the best recovery in the South Africa, Botswana, Namibia, and southern Tanzania. The maximum amplitude of the input anomalies is not fully recovered, with both the *P* wave and *S* wave models recovering ~30–40% of the input amplitudes, but this is consistent with other body wave tomography studies using relative arrival-time data (Bastow et al., 2005). Station static terms are removed during the inversion to account for structure at <50 km depth, where ray crossing is minimal. The distribution of station static terms is centered at the origin with a standard deviation of 0.36 s. Negative station static terms are generally correlated with regions of Archean crust and positive station static terms are correlated with regions outside the Kalahari Craton (Figure S8). For the checkerboard models, the station terms are comparable (~0.2 s), and with respect to the rms travel-time residual reduction in the models, the station static terms account for ~5% of the reduction.

7. Discussion

To summarize, the *P* wave and *S* wave models are similar and show several anomalies in the upper mantle seen in previous body wave velocity models, as well as several new anomalies (Table 1). We first discuss anomalies that have been imaged previously in regional body wave models (as reviewed in section 3), and then discuss the new anomalies.

7.1. Anomalies Reported in Previous Studies

The Kaapvaal Craton has higher than average seismic velocities in the upper 400 km (Anomaly A, Figures 3a, 3f, 4a, and 4f). Beneath the Kaapvaal Craton, a region of lower than average velocity (Anomaly B, Figures 3a and 3f) is present under the Bushveld Complex, and extends to the northwest into central Botswana. Within the Damara Belt in northwestern Botswana, there are lower than average velocities (Anomaly C, Figures 3a–3c) in the upper mantle under the ORZ. To the south of the Kaapvaal Craton, in the Namaqua-Natal Belt, the velocity structure is nearly average, with slightly lower than average velocity structure near the Gariep Belt and slightly higher than average velocities in a region directly south of the Kheis Belt. There is a low velocity anomaly beneath the Cape Fold Belt.

As argued by Ortiz et al. (2019), the higher than average velocities beneath the greater Kalahari Craton, including portions of the Okwa Terrane and Magondi Belt, are consistent with the northwestern margin of the Kalahari Craton aligning with the southern boundary of the Damara Belt in northern Botswana and Namibia. Also noted by Ortiz et al. (2019), the low velocity anomaly (Anomaly B) beneath the Bushveld Complex and central Botswana indicates that the upper mantle in this region may have been altered by the Bushveld or other large Precambrian magmatic events.

At the southwestern terminus of the EARS, Yu et al. (2017) imaged a −1% Vp anomaly between ~150 and 300 km depth beneath the ORZ. The amplitude and depth extent of the LVZ they imaged is similar to the low velocity anomaly imaged beneath the ORZ in our model (Figures 2, S3, and S4). Yu et al. (2017) attributed the anomaly in their model to a reduction of upper mantle velocity caused by decompression melting associated with thinning of the lithosphere. In our model, we show that this anomaly is not constrained laterally to the upper mantle beneath the ORZ, but is part of a larger anomaly present beneath most of the Damara Belt.

Beneath the Damara Belt in southern and central Zambia, our models also show a previously reported, deep-seated upper mantle low velocity anomaly (Anomaly D, Figures 3a and 3b). Our model is consistent with the Mulibo and Nyblade (2013a, 2013b) studies, which attributed this anomaly to a whole-mantle, thermochemical structure (i.e., the African Superplume) extending from the lower mantle beneath southern Africa to the upper mantle beneath eastern Africa.

At the northernmost edge of our model, the western side of the Bangweulu Block is characterized by lower than average velocities in the upper 400 km. To the southeast, beneath the eastern side of the Bangweulu Block and the Irumide Belt, higher than average velocities (Anomaly E, Figures 3a and 3b) are imaged in the upper 400 km. This transition between lower than average velocities beneath the western side of the Bangweulu Block and higher than average velocities beneath the Irumide Belt was seen previously in the body wave tomography models reported by Mulibo and Nyblade (2013a) and Grijalva et al. (2018).

7.2. New Anomalies

Outside of the footprint of previous regional body wave investigations, our models reveal several new anomalies (Anomalies F, G, H, I, and J; Figures 3 and 4). To further investigate the spatial and depth extent of these anomalies, several tabular body resolution tests (Figures 7 and 8) have been conducted using the same inversion parameters as in the model (Figures 2, 3, and 4). For these tests, we created velocity anomalies to represent a difference in lithospheric thickness between cratonic and noncratonic lithosphere, as well as thermal anomalies of unspecified origin but possibly linked to the African Superplume, within the lithosphere and deeper in the upper mantle. The velocity anomalies were created similar to the checkers in the checkerboard resolution tests using cylinders and a Gaussian velocity distribution. A maximum velocity change was applied over a proscribed depth interval, and a fall-off to the half-maximum velocity was set to 50 km above and below that interval. Below we discuss the new anomalies along with the results of the tabular body resolution tests.

Within the Damara Belt, previously imaged low velocity anomalies beneath the ORZ (Anomaly C; Yu et al., 2017; Ortiz et al., 2019) are part of a more extensive low velocity anomaly beneath most of the Damara Belt (Anomaly F, Figures 3a and 3b). Anomaly F is present in both the *P* wave and *S* wave models in the upper 400 km, extending from the central Namibian coast to the ORZ. Almost the entire upper mantle beneath the Damara Belt has lower than average velocity structure. The southern boundary of Anomalies C and F track remarkably well with the mapped southern boundary of the Damara Belt within Namibia and Botswana (Figure 3a), providing additional strong evidence that the southern edge of the Damara Belt marks the northwestern boundary of the greater Kalahari Craton, as argued by Ortiz et al. (2019).

To test if the broad anomaly beneath the Damara Belt can be attributed to differences in lithospheric thickness, or if thermal anomalies in the upper mantle need to be invoked to explain it, we examine tabular body test results for thinner lithosphere beneath the Damara Belt juxtaposed with thicker cratonic lithosphere (Figures 7d and 8d), and then for a series of upper mantle thermal anomalies at different depths (Figures 7a, 7g, 7j, 7m and 8a, 8g, 8j, 8m). In these tabular body tests, low velocity structures are also placed in the upper mantle beneath southern Zambia and in the lower mantle beneath central Zambia to account for the African Superplume structure that gives rise to those anomalies (Anomalies D and K).

For investigating the difference in lithospheric thickness between thinner mobile belt lithosphere and thicker cratonic lithosphere, model parameters were selected based on the depth of the conductive lithosphere determined using mantle xenolith data (Janney et al., 2010) (Figures 7d and 8d). The base of the mobile belt lithosphere was set to 130 km and the base of the cratonic lithosphere was set to 200 km depth. A contrast in lithospheric thickness of ~70 km (i.e., 130 vs. 200 km) in this region is consistent with continental-scale surface wave tomography studies (e.g., Emry et al., 2019; Fishwick, 2010; Priestley et al.,

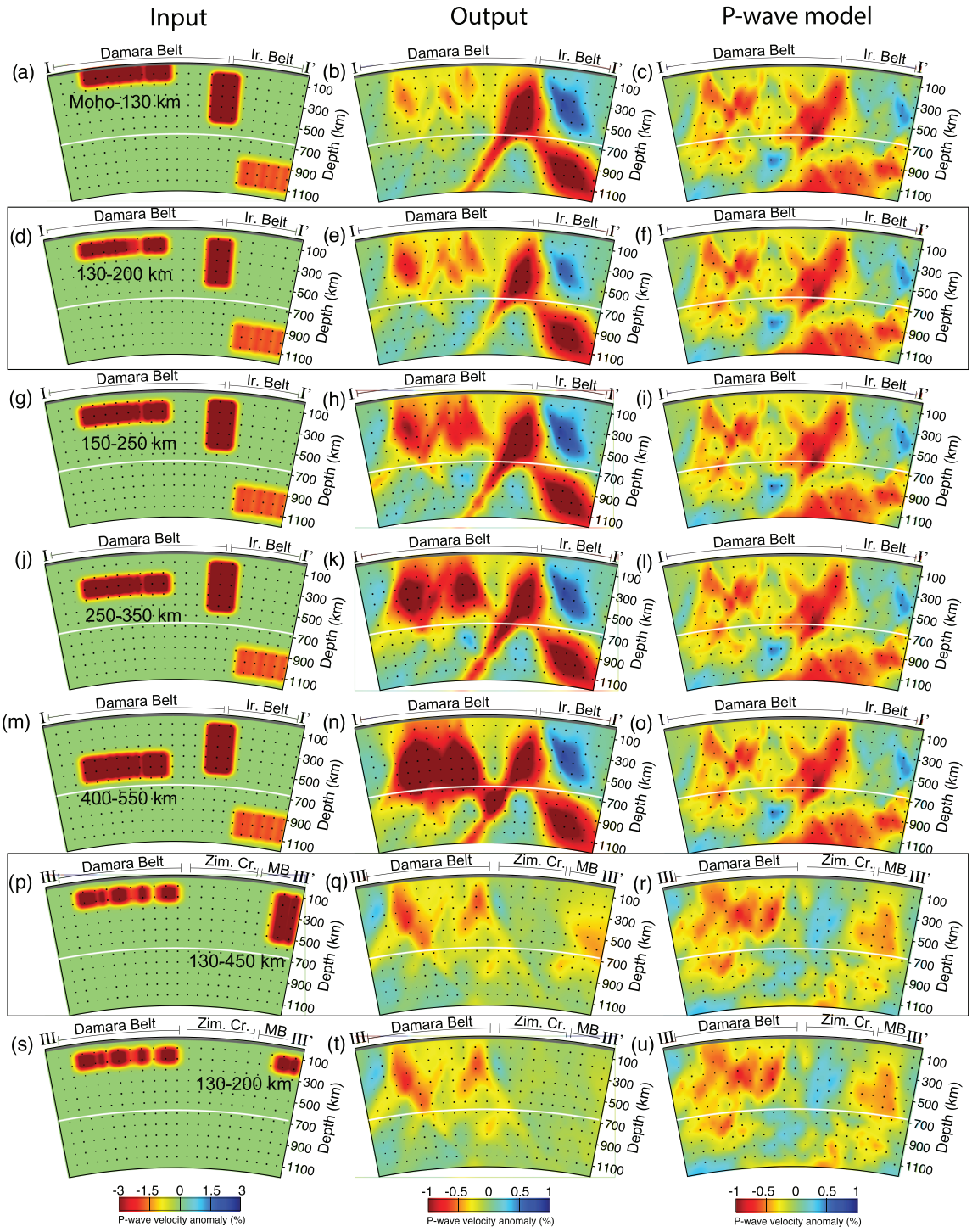

Figure 7. (left column) Tabular body models (input) for profiles I-I′ and III-III′ shown in Figures 3a and 3d used to create a synthetic *P* wave travel-time data set. (a, d, g, j, m, p, s) Thermal anomalies in the mantle beneath the Damara Belt. (d) An anomaly representing relatively thin lithosphere (~130 km) beneath the Damara Belt adjacent to relatively thick lithosphere (~200 km) beneath the Kalahari Craton. (p, s) Thermal anomalies in the mantle beneath the Mozambique Belt. (middle column: b, e, h, k, n, q, t) Recovered tabular body models. (right column: c, f, i, l, o, r, u) Synthetic models used for interpretation are outlined with black boxes. *P* wave model (same as Figures 3a and 3d) for comparison. Ir = Irumide; Zim. Cr. = Zimbabwe Craton; MB = Mozambique Belt.

2008). The velocity anomaly within the 130–200 km depth range was constrained by the difference in temperature between the cratonic geotherm and the mantle adiabat at the depth midpoint between the base of the cratonic lithosphere and the base of the mobile belt lithosphere (i.e., 165 km). The

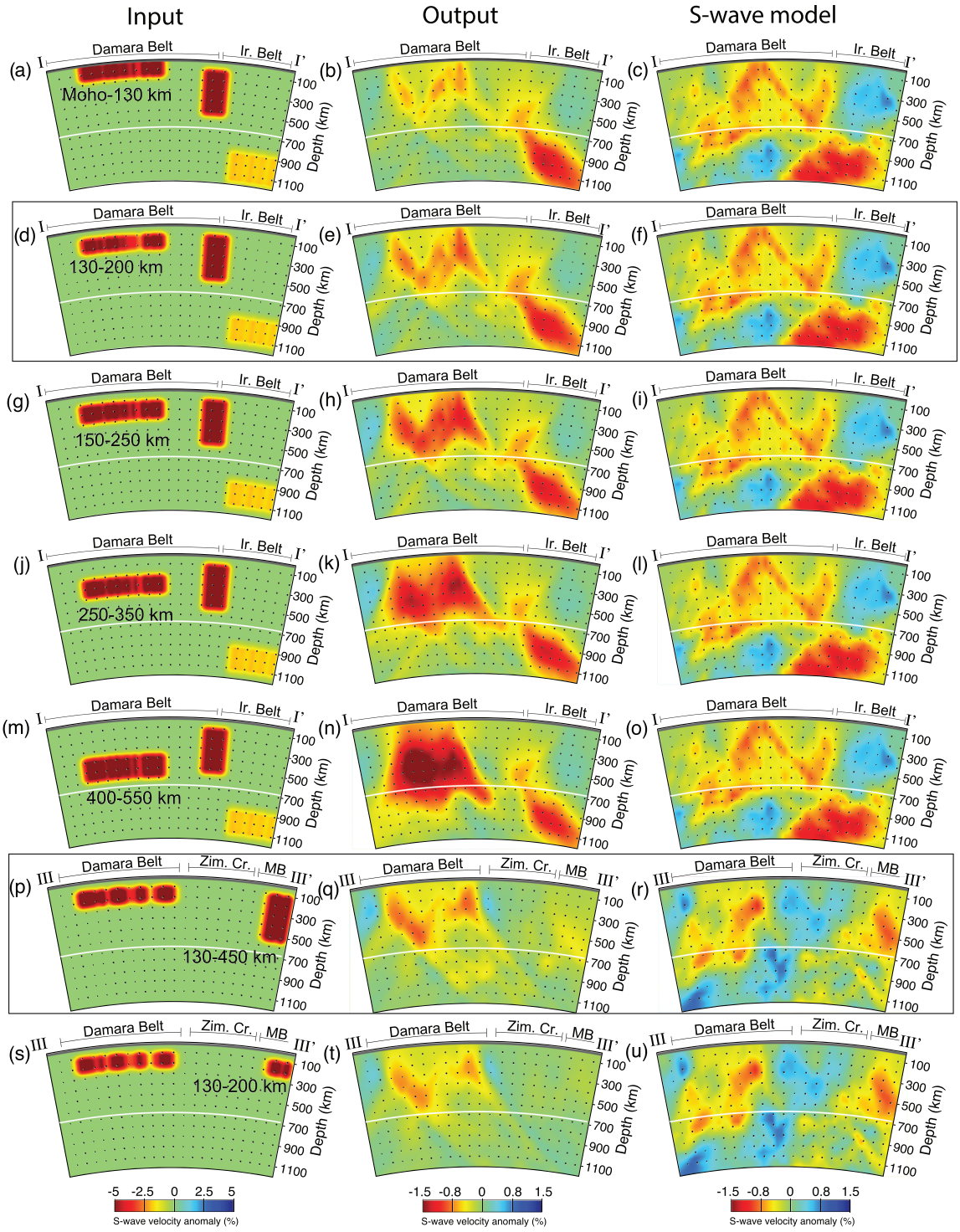

Figure 8. (left column) Tabular body models (input) for profiles I-I′ and III-III′ shown in Figures 4a and 4d used to create a synthetic *S* wave travel-time data set. (a, d, g, j, m, p, s) Thermal anomalies in the mantle beneath the Damara Belt. (d) An anomaly representing relatively thin lithosphere (~130 km) adjacent to relatively thick lithosphere (~200 km) beneath the Damara Belt. (p, s) Thermal anomalies in the mantle beneath the Mozambique Belt. (middle column: b, e, h, k, n, q, t) Recovered tabular body models. (right column: c, f, i, l, o, r, u) Synthetic models used for interpretation are outlined with black boxes. *P* wave model (same as Figures 4a and 4d) for comparison. Ir = Irumide; Zim. Cr. = Zimbabwe Craton; MB = Mozambique Belt.

temperature difference (~250–300 K) was then converted to *P* wave and *S* wave velocities following the velocity-temperature relationships in Cammarano et al. (2003). This yielded velocity differences of ~2.25% for Vp and ~3.9% for Vs. However, because mantle velocity is also sensitive to the difference in composition between cratonic lithosphere and sublithospheric mantle (Jordan, 1979; Schutt & Lesher, 2010), maximum *P* wave velocity anomalies of 4% and *S* wave velocity anomalies of 6% were used for tabular body models. These anomalies are within the range of synthetic tests used by other studies for southern and eastern Africa (Grijalva et al., 2018; Mulibo & Nyblade, 2013a; Ortiz et al., 2019). Maximum velocity anomalies of −4% and −6% for Vp and Vs, respectively, were also used for investigating the possibility of a shallow lithospheric thermal anomaly between depths of 40 and 130 km (Figures 7a and 8a), and for the deep upper mantle thermal anomalies between depths of 150 and 250 km (Figures 7g and 8b), 250 and 350 km (Figures 7j and 8j), and 400 and 550 km (Figures 7m and 8m).

Results of the synthetic tests show that within the Damara Belt, from the ORZ to the Namibian coast, thin lithosphere (i.e., 130 vs. 200 km) can account for the majority of the anomalous velocity in the model (Figures 7d–7f and 8d–8f), with the exception of a deeper anomaly in northernmost Namibia. In comparison, the results of the tabular body tests with low velocity anomalies in the lithosphere (Figures 7a–7c and 8a–8c) or else deeper in the upper mantle (Figures 7g–7o and 8g–8o) do not provide as good of a match to the model results. We therefore attribute the low velocity anomaly in the upper 400 km along the Damara Belt (Anomaly F, Figures 3a and 3f), including the anomaly beneath the ORZ, to a difference in mobile belt versus craton lithospheric thickness and argue that thermally perturbed upper mantle, possibly linked to lithospheric rifting and/or the lower mantle African Superplume structure, does not need to be invoked to explain Anomalies C and F.

In both the *P* wave and *S* wave models, at depths between 500 and 800 km, there is a low velocity anomaly beneath northernmost Namibia and southern Angola (Figures 3e, S3, and S4). This anomaly lies along the northern edge of our model where resolution degrades. A low velocity anomaly in the upper mantle beneath southern Angola has been imaged using ambient noise tomography (Emry et al., 2019). Emry et al. (2019) associated this anomaly to the Angola (Bie) Dome. Our results suggest that the upper mantle anomaly imaged by Emry et al. (2019) under the Bie Dome may extend as deep as or even deeper than the transition zone over a fairly large area extending into northern Namibia.

Anomaly F in the Damara Belt has an abrupt western boundary in northern Namibia. West of Anomaly F, there is a region of higher than average velocity (Anomaly G; Figures 3a and 3d) in the upper 300 km along the northwestern Namibian coast. Receiver functions from this region have been interpreted to show a thick, depleted lithospheric mantle beneath the Etendeka Flood Basalt Province (Yuan et al., 2017). Depleted and thicker lithosphere under this region, resulting from the interaction with the Tristan Da Cunha mantle plume, would result in an upper mantle with seismic velocities that are higher than the surrounding region. Following Yuan et al. (2017), we attribute the higher than average velocities of Anomaly G to localized lithospheric alteration from the Etendeka magmatic event. An alternative interpretation, however, is that a lobe of thicker cratonic lithosphere extends south from the Angolan shield beneath northwestern Namibia.

In general, the Rehoboth Province is characterized by higher than average seismic velocity (Anomaly H, Figures 3a, 3c, and 3e) within our models. In addition to Archean-age detrital zircons collected in the Rehoboth Province (van Schijndel et al., 2011) and high resistivity structure extending to a depth of ~180 km (Muller et al., 2009), the higher than average velocities within Anomaly H suggest that some portion of the Rehoboth lithosphere is cratonic and predates the amalgamation of the Rehoboth Province with the Kaapvaal Craton during the Paleoproterozoic. One possibility is that the faster than average structure (Anomaly H) is part of the Archean Maltahohe Microcraton (Begg et al., 2009). The velocities beneath the Rehoboth Province increase from west-to-east, suggesting that some alteration of the craton-like lithosphere could have occurred along the western boundary with the Damara Belt during the Pan-African orogeny.

Within central Mozambique, there is a low velocity anomaly (Anomaly I) that extends from the surface to 700 km depth (Figures 3a and 3d). It is clear that the EARS extends southward into the Mozambique Belt in central Mozambique. For example, Fonseca et al. (2014) showed a continuation of active seismicity from the Malawi Rift south along the Urema Graben into central Mozambique, and using the MOZART data, Domingues et al. (2016) correlated a boundary in crustal velocity with active seismicity that continues all the way into southern Mozambique. In the 500 km depth slice (Figure S3), Anomaly I looks very similar

to the deep-seated anomaly beneath southern Zambia (Anomaly D, Figures 3a, 3b, and 3c); however, we note that Anomaly I is present in an area of the model with limited resolution (Figure 5).

In Figures 7p–7u and 8p–8u we show synthetic tabular body tests assessing the possible sources of the anomalous velocities beneath central Mozambique. In these tests, a velocity anomaly between 130 and 200 km depth has been used to simulate the difference in lithospheric thickness between the Mozambique Belt and Zimbabwe Craton (Figures 7p and 8p) and an anomaly that extends deeper into the upper mantle to simulate a deep-seated thermal anomaly (−4% Vp; −6% Vs) (Figures 7s and 8s). Results of these tests indicate that thin lithosphere alone (Figures 7s–7u and 8s–8u) cannot account for the structure imaged between 400 and 700 km depth in the model (Figures 7r, 7u, 8r, and 8u), and that additional structure extending to >200 km depth is required to provide a good match to the model (Figures 7p–7r and 8p–8r). In addition, recovery of the 6% synthetic anomaly in the *S* wave model (Figures 8p–8r) indicates that the anomaly may have a larger magnitude in Vs. We suggest that the upper mantle in this region is thermally perturbed to depths ≥200 km, and that the perturbation could be geodynamically linked to the African Superplume structure in the lower mantle.

No mapped portions of the Congo Craton or Angolan Shield lie within the footprint of seismic stations used in this study. However, a region of higher than average velocity is present near the northwestern boundary of the ORZ. High resistivity (Bufford et al., 2012) and high seismic velocity (Yu et al., 2017) upper mantle, along with crustal thickening (Fadel et al., 2018), all point toward the southern boundary of the Congo Craton extending into northwestern Botswana along the northwestern boundary of the ORZ. Our models support this conclusion, namely, that the southern boundary of the Congo Craton may extend to the south along the northwestern edge of the ORZ.

Beneath a large portion of the Southern Irumide Belt, velocities in the upper 400 km are higher than average (Anomaly J, Figure 3a) and comparable in amplitude to the velocities imaged beneath the southern Kaapvaal Craton (Anomaly A). Several arguments have recently been made for the presence of craton-like lithosphere beneath the Southern Irumide Belt, based on a suite of geophysical evidence. Adams et al. (2018) imaged fast structure beneath the Irumide and Southern Irumide Belts, but were unable to distinguish structure between the two belts. Using ambient noise tomography, Emry et al. (2019) imaged fast velocity structure in the upper ~230 km beneath the Southern Irumide Belt and argued for the presence of at least two cratonic fragments (i.e., the Niassa and Lurio Cratons). Modeling lithospheric thickness using magnetotelluric and aeromagnetic data, Sarafian et al. (2018) show thinner (~120 km) lithosphere separating thicker (~150 km) lithosphere beneath the Irumide Belt and even thicker (>200 km) lithosphere beneath the Southern Irumide Belt. We therefore attribute the higher than average velocities (Anomaly J) beneath the Southern Irumide Belt to a cratonic fragment, possibly the Niassa Craton.

7.3. Uplift of the Southern African Plateau

Our results can be used to address the question raised in section 1 about whether the upper mantle beneath southern Africa shows signs of thermal modification that could provide a source of buoyancy for the Southern African Plateau. While there is a prominent low velocity anomaly in the upper mantle beneath the Damara Belt, our resolution tests show that a ~4% Vp contrast, focused at depths between 130 and 200 km (depths consistent with plausible lithospheric thickness variations), can explain the anomalous velocities beneath the Damara Belt. Therefore, there is no need to invoke a thermal anomaly in the upper mantle. However, we cannot rule one out.

Beneath central Mozambique, on the other hand, Anomaly I in our models cannot be fully explained by differences in lithospheric thickness alone, indicating that the upper mantle may be thermally perturbed, and that the perturbation may be associated with the lower mantle African Superplume. From these findings, we argue that the source of buoyancy support for the excess elevations of the Southern African Plateau need not arise from thermally perturbed upper mantle and more likely derives from middle-to-lower mantle structure. Interestingly, while much of central and southern Mozambique lacks anomalously high topography, compared to the rest of southern Africa, the African Superplume anomaly may be providing additional heat to the upper mantle beneath the Mozambique Belt in central Mozambique, as well as beneath parts of Zambia and to the north beneath East Africa.

8. Summary and Conclusions

In summary, the *P* wave and *S* wave velocity structure in our models is consistent with other models in regions imaged previously using regional body wave tomography. For example, the upper mantle velocities in our models beneath the Kaapvaal Craton, Limpopo Belt, Zimbabwe Craton, and portions of the Okwa and Magondi Belts (i.e., the greater Kalahari Craton) are higher than average (Anomaly A) and comparable to models from previous studies (e.g., Fouch et al., 2004; James et al., 2001; Ortiz et al., 2019; Youssof et al., 2015). Our models support the results of Ortiz et al. (2019), who suggested that the Okwa and Magondi Belts are underlain by thick cratonic lithosphere and are therefore part of the greater Kalahari Craton. In this interpretation, the southern boundary of the Damara Belt marks the northern margin of the Kalahari Craton.

A low velocity anomaly is present beneath the Bushveld Complex, extending to the northwest into central Botswana, as reported by Ortiz et al. (2019) (Anomaly B). The velocity structure beneath the Namaqua-Natal Belt is nearly average and the upper 400 km beneath the Cape Fold Belt is lower than average, similar to the Ortiz et al. (2019) and Fouch et al. (2004) models. Consistent with previous investigations (i.e., Mulibo & Nyblade, 2013a, 2013b; Ortiz et al., 2019), there is a deep-seated low velocity anomaly (Anomaly D) beneath southern and central Zambia that extends at least as deep as the mantle transition zone. Beneath the ORZ, a low velocity anomaly is present in the upper 400 km of the mantle (Anomaly C), similar to the anomaly imaged by Yu et al. (2017), and is spatially separated from the low velocity anomaly beneath the Bushveld Complex and central Botswana at depths below 100 km (Anomaly B).

There are several new anomalies in our models in regions that have not been imaged previously by body wave tomography. Extending to the southwest from the ORZ in the Damara Belt in northern Namibia, there is a low velocity anomaly (Anomaly F) in the upper 400 km of the mantle. Together, Anomalies F and C can be explained by thinner lithosphere (~130 km) beneath the Damara Belt compared to thick, cratonic lithosphere (~200 km) to the south. A thermal perturbation in the upper mantle either from Cenozoic rifting under the ORZ or the African Superplume is not required to explain the combined Anomalies F and C. To the west of the Damara Belt, in northwestern Namibia, there is a high velocity anomaly (Anomaly G) beneath the Etendeka Flood Basalt Province. This anomaly can be explained by the lithosphere altered by Cretaceous magmatism, or from a southern lobe of thick Congo Craton lithosphere. The upper mantle velocity structure beneath the Rehoboth Province is higher than average (Anomaly H) and may reflect the presence of a cratonic fragment, the Maltahohe Microcraton, comprising at least part of the province. A deep-seated low velocity anomaly (Anomaly I) is present beneath the Mozambique Belt in central Mozambique, with a similar depth extent to the low velocity anomaly beneath southern and central Zambia. Thinner lithosphere compared to the adjacent cratons in this region cannot fully explain the depth extent of Anomaly I, indicating the presence of an upper mantle thermal anomaly possibly linked to the lower mantle African Superplume structure. A high velocity anomaly (Anomaly J) is located to the north of Anomaly I within the Southern Irumide Belt. In addition to Anomaly J in our models, other lines of geophysical evidence indicate the presence of cratonic lithosphere (the Niassa Craton) in this region (Adams et al., 2018; Emry et al., 2019; Sarafian et al., 2018).

With regard to the origin of the Southern African Plateau, our findings suggest that the source of buoyancy for the excess elevations of the plateau do not likely reside at upper mantle depths but instead arise from middle-to-lower mantle structure. High velocity upper mantle structure is found beneath much of the Southern African Plateau, and in places like the Damara Belt where lower velocity structure is present, the velocity reduction in the upper mantle can be simply explained by variations in lithosphere thickness. Thermal anomalies in the upper mantle do not need to be invoked to explain the velocity structure of the upper mantle under the Damara Belt.

Acknowledgments

The sources of data used in this study are listed in section 4. We would like to thank colleagues at the Namibia Geological Survey and the IRIS PASSCAL Instrument Center for help with installing and operating the 2015–2018 Africa Array Namibia seismic network and the Botswana Geological Survey for installing and maintaining the NARS-Botswana network. We would also like to thank Stewart Fishwick and an anonymous reviewer for constructive and helpful comments, Ian Bastow for helpful discussions about modeling procedures, and Joao Fonseca and George Helffrich for providing data from the MOZART project. This work was supported by Grant ALW-GO-AO/11-30 from the Nederlandse Organisatievoor Wetenschappelijk Onderzoek (NWO) and Grants 0440032, 0530062, 0824781, 1128936, and 1634108 from the National Science Foundation. Data used in this study can be obtained from the IRIS Data Management Center (https://ds.iris.edu/ds/).

Data Availability Statement

The sources of data used in this study are listed in section 4.

References

Accardo, N. J., Shillington, D. J., Gaherty, J. B., Scholz, C. A., Nyblade, A. A., Chindandali, P. R. N., et al. (2018). Constraints on rift basin structure and border fault growth in the northern Malawi rift from 3-D seismic refraction imaging. *Journal of Geophysical Research: Solid Earth*, *123*, 10,003–10,025. https://doi.org/10.1029/2018JB016504

Adams, A., Miller, J., & Accardo, N. (2018). Relationships between lithospheric structures and rifting in the East African Rift System: A Rayleigh wave tomography study. *Geochemistry, Geophysics, Geosystems*, *19*(10), 3793–3810. https://doi.org/10.1029/2018GC007750

Adams, A., & Nyblade, A. (2011). Shear wave velocity structure of the southern African upper mantle with implications for the uplift of southern Africa. *Geophysical Journal International*, *186*(2), 808–824. https://doi.org/10.1111/j.1365-246X.2011.05072.x

Adams, A., Nyblade, A., & Weeraratne, D. (2012). Upper mantle shear wave velocity structure beneath the East African plateau: Evidence for a deep, plateauwide low velocity anomaly. *Geophysical Journal International*, *189*(1), 123–142. https://doi.org/10.1111/j.1365-246X.2012.05373.x

Anhaeusser, C. R. (1973). A discussion on the evolution of the Precambrian crust—The evolution of the early Precambrian crust of southern Africa. *Philosophical Transactions of the Royal Society of London Series A, Mathematical and Physical Sciences*, *273*(1235), 359–388. https://doi.org/10.1098/rsta.1973.0006

Bagley, B., & Nyblade, A. A. (2013). Seismic anisotropy in eastern Africa, mantle flow, and the African superplume. *Geophysical Research Letters*, *40*(8), 1500–1505. https://doi.org/10.1002/grl.50315

Bastow, I. D., Stuart, G. W., Kendall, J. M., & Ebinger, C. J. (2005). Upper-mantle seismic structure in a region of incipient continental breakup: Northern Ethiopian rift. *Geophysical Journal International*, *162*(2), 479–493. https://doi.org/10.1111/j.1365-246X.2005.02666.x

Batumike, J. M., Griffin, W. L., O'Reilly, S. Y., Belousova, E. A., & Pawlitschek, M. (2009). Crustal evolution in the central Congo-Kasai Craton, Luebo, DR Congo: Insights from zircon U–Pb ages, Hf-isotope and trace-element data. *Precambrian Research*, *170*(1–2), 107–115. https://doi.org/10.1016/j.precamres.2008.12.001

Bauer, K., Neben, S., Schreckenberger, B., Emmermann, R., Hinz, K., Fechner, N., et al. (2000). Deep structure of the Namibia continental margin as derived from integrated geophysical studies. *Journal of Geophysical Research*, *105*(B11), 25,829–25,853. https://doi.org/10.1029/2000JB900227

Begg, G. C., Griffin, W. L., Natapov, L. M., O'Reilly, S. Y., Grand, S. P., O'Neill, C. J., et al. (2009). The lithospheric architecture of Africa: Seismic tomography, mantle petrology, and tectonic evolution. *Geosphere*, *5*(1), 23–50. https://doi.org/10.1130/GES00179.1

Brock, B. B. (1959). On orogenic evolution, with special reference to southern Africa. *South African Journal of Geology*, *62*(1), 325–372.

Bufford, K. M., Atekwana, E. A., Abdelsalam, M. G., Shemang, E., Atekwana, E. A., Mickus, K., et al. (2012). Geometry and faults tectonic activity of the Okavango Rift Zone, Botswana: Evidence from magnetotelluric and electrical resistivity tomography imaging. *Journal of African Earth Sciences*, *65*, 61–71. https://doi.org/10.1016/j.jafrearsci.2012.01.004

Cammarano, F., Goes, S., Vacher, P., & Giardini, D. (2003). Inferring upper-mantle temperatures from seismic velocities. *Physics of the Earth and Planetary Interiors*, *138*(3–4), 197–222. https://doi.org/10.1016/S0031-9201(03)00156-0

Chevrot, S., & Zhao, L. (2007). Multiscale finite-frequency Rayleigh wave tomography of the Kaapvaal craton. *Geophysical Journal International*, *169*(1), 201–215. https://doi.org/10.1111/j.1365-246X.2006.03289.x

Cornell, D. H., Van Schijndel, V., Ingolfsson, O., Scherstén, A., Karlsson, L., Wojtyla, J., & Karlsson, K. (2011). Evidence from Dwyka tillite cobbles of Archaean basement beneath the Kalahari sands of southern Africa. *Lithos*, *125*(1–2), 482–502. https://doi.org/10.1016/j.lithos.2011.03.006

de Wit, M. J., Jones, M. G., & Buchanan, D. L. (1992). The geology and tectonic evolution of the Pietersburg greenstone belt, South Africa. *Precambrian Research*, *55*(1–4), 123–153. https://doi.org/10.1016/0301-9268(92)90019-K

Domingues, A., Silveira, G., Ferreira, A. M., Chang, S. J., Custódio, S., & Fonseca, J. F. (2016). Ambient noise tomography of the East African Rift in Mozambique. *Geophysical Journal International*, *204*(3), 1565–1578. https://doi.org/10.1093/gji/ggv538

Duncan, R. A., Hooper, P. R., Rehacek, J., Marsh, J., & Duncan, A. R. (1997). The timing and duration of the Karoo igneous event, southern Gondwana. *Journal of Geophysical Research*, *102*(B8), 18,127–18,138. https://doi.org/10.1029/97JB00972

Eglington, B. M. (2006). Evolution of the Namaqua-Natal Belt, southern Africa—A geochronological and isotope geochemical review. *Journal of African Earth Sciences*, *46*(1–2), 93–111. https://doi.org/10.1016/j.jafrearsci.2006.01.014

Emry, E. L., Shen, Y., Nyblade, A. A., Flinders, A., & Bao, X. (2019). Upper mantle Earth structure in Africa from full-wave ambient noise tomography. *Geochemistry, Geophysics, Geosystems*, *20*, 120–147. https://doi.org/10.1029/2018GC007804

Fadel, I., van der Meijde, M., & Paulssen, H. (2018). Crustal structure and dynamics of Botswana. *Journal of Geophysical Research: Solid Earth*, *123*, 10,659–10,671. https://doi.org/10.1029/2018JB016190

Fishwick, S. (2010). Surface wave tomography: Imaging of the lithosphere–asthenosphere boundary beneath central and southern Africa? *Lithos*, *120*(1–2), 63–73. https://doi.org/10.1016/j.lithos.2010.05.011

Fonseca, J. F. B. D., Chamussa, J., Domingues, A., Helffrich, G., Antunes, E., van Aswegen, G., et al. (2014). MOZART: A seismological investigation of the East African rift in Central Mozambique. *Seismological Research Letters*, *85*(1), 108–116. https://doi.org/10.1785/0220130082

Forsyth, D. W., & Li, A. (2005). Array analysis of two-dimensional variations in surface wave phase velocity and azimuthal anisotropy in the presence of multipathing interference. *Seismic Earth: Array Analysis of Broadband Seismograms*, *157*, 81–97. https://doi.org/10.1029/157GM06

Forte, A. M., Quéré, S., Moucha, R., Simmons, N. A., Grand, S. P., Mitrovica, J. X., & Rowley, D. B. (2010). Joint seismic–geodynamic-mineral physical modelling of African geodynamics: A reconciliation of deep-mantle convection with surface geophysical constraints. *Earth and Planetary Science Letters*, *295*(3–4), 329–341. https://doi.org/10.1016/j.epsl.2010.03.017

Fouch, M. J., James, D. E., VanDecar, J. C., Van der Lee, S., & Kaapvaal Seismic Group (2004). Mantle seismic structure beneath the Kaapvaal and Zimbabwe Cratons. *South African Journal of Geology*, *107*(1–2), 33–44. https://doi.org/10.2113/107.1-2.33

Frimmel, H. E., & Frank, W. (1998). Neoproterozoic tectono-thermal evolution of the Gariep Belt and its basement, Namibia and South Africa. *Precambrian Research*, *90*(1–2), 1–28. https://doi.org/10.1016/S0301-9268(98)00029-1

Gilfillan, S. M. V., Györe, D., Flude, S., Johnson, G., Bond, C. E., Hicks, N., et al. (2019). Noble gases confirm plume-related mantle degassing beneath southern Africa. *Nature Communications*, *10*(1), 5028–5027. https://doi.org/10.1038/s41467-019-12944-6

Grijalva, A., Nyblade, A. A., Homman, K., Accardo, N. J., Gaherty, J. B., Ebinger, C. J., et al. (2018). Seismic evidence for plume-and craton-influenced upper mantle structure beneath the northern Malawi Rift and the Rungwe Volcanic Province, East Africa. *Geochemistry, Geophysics, Geosystems*, *19*(10), 3980–3994. https://doi.org/10.1029/2018GC007730

Gurnis, M., Mitrovica, J. X., Ritsema, J., & van Heijst, H. J. (2000). Constraining mantle density structure using geological evidence of surface uplift rates: The case of the African superplume. *Geochemistry, Geophysics, Geosystems*, *1*(7). https://doi.org/10.1029/1999GC000035

Hansen, S. E., Nyblade, A. A., & Benoit, M. H. (2012). Mantle structure beneath Africa and Arabia from adaptively parameterized *P*-wave tomography: Implications for the origin of Cenozoic Afro-Arabian tectonism. *Earth and Planetary Science Letters*, *319-320*, 23–34. https://doi.org/10.1016/j.epsl.2011.12.023

Hansma, J., Tohver, E., Schrank, C., Jourdan, F., & Adams, D. (2016). The timing of the Cape Orogeny: New 40Ar/39Ar age constraints on deformation and cooling of the Cape Fold Belt, South Africa. *Gondwana Research*, *32*, 122–137. https://doi.org/10.1016/j.gr.2015.02.005

Hanson, R. E. (2003). Proterozoic geochronology and tectonic evolution of southern Africa. *Geological Society, London, Special Publications*, *206*(1), 427–463. https://doi.org/10.1144/GSL.SP.2003.206.01.20

James, D. E., Fouch, M. J., VanDecar, J. C., Van Der Lee, S., & Kaapvaal Seismic Group (2001). Tectospheric structure beneath southern Africa. *Geophysical Research Letters*, *28*(13), 2485–2488. https://doi.org/10.1029/2000GL012578

Janney, P. E., Shirey, S. B., Carlson, R. W., Pearson, D. G., Bell, D. R., Le Roex, A. P., et al. (2010). Age, composition and thermal characteristics of south African off-craton mantle lithosphere: Evidence for a multi-stage history. *Journal of Petrology*, *51*(9), 1849–1890. https://doi.org/10.1093/petrology/egq041

Jelsma, H. A., & Dirks, P. H. (2002). Neoarchaean tectonic evolution of the Zimbabwe Craton. *Geological Society, London, Special Publications*, *199*(1), 183–211. https://doi.org/10.1144/GSL.SP.2002.199.01.10

Jordan, T. H. (1979). Mineralogies, densities and seismic velocities of garnet lherzolites and their geophysical implications. *The Mantle Sample: Inclusion in Kimberlites and Other Volcanics*, *16*, 1–14. https://doi.org/10.1029/SP016p0001

Kachingwe, M., Nyblade, A., & Julia, J. (2015). Crustal structure of Precambrian terranes in the southern African subcontinent with implications for secular variation in crustal genesis. *Geophysical Journal International*, *202*(1), 533–547. https://doi.org/10.1093/gji/ggv136

Kennett, B. L. N., & Engdahl, E. R. (1991). Traveltimes for global earthquake location and phase identification. *Geophysical Journal International*, *105*(2), 429–465. https://doi.org/10.1111/j.1365-246X.1991.tb06724.x

Kgaswane, E. M., Nyblade, A. A., Julià, J., Dirks, P. H., Durrheim, R. J., & Pasyanos, M. E. (2009). Shear wave velocity structure of the lower crust in southern Africa: Evidence for compositional heterogeneity within Archaean and Proterozoic terrains. *Journal of Geophysical Research*, *114*, B12304. https://doi.org/10.1029/2008JB006217

Khoza, D., Jones, A. G., Muller, M. R., Evans, R. L., Webb, S. J., & Miensopust, M. (2013). Tectonic model of the Limpopo belt: Constraints from magnetotelluric data. *Precambrian Research*, *118*(8), 4378–4397. https://doi.org/10.1002/jgrb.50258

Kröner, A. (1977). The Precambrian geotectonic evolution of Africa: Plate accretion versus plate destruction. *Precambrian Research*, *4*(2), 163–213. https://doi.org/10.1016/0301-9268(77)90045-6

Kwadiba, M. T. O. G., Wright, C., Kgaswane, E. M., Simon, R. E., & Nguuri, T. K. (2003). Pn arrivals and lateral variations of Moho geometry beneath the Kaapvaal craton. *Lithos*, *71*(2–4), 393–411. https://doi.org/10.1016/j.lithos.2003.07.008

Li, A., & Burke, K. (2006). Upper mantle structure of southern Africa from Rayleigh wave tomography. *Journal of Geophysical Research*, *111*, B10303. https://doi.org/10.1029/2006JB004321

Li, A., & Li, L. (2015). Love wave tomography in southern Africa from a two-plane-wave inversion method. *Geophysical Journal International*, *202*(2), 1005–1020. https://doi.org/10.1093/gji/ggv203

Lithgow-Bertelloni, C., & Silver, P. G. (1998). Dynamic topography, plate driving forces and the African superswell. *Nature*, *395*(6699), 269. https://doi.org/10.1038/26212

McCourt, S., Hilliard, P., Armstrong, R. A., & Munyanyiwa, H. (2001). SHRIMP U-Pb zircon geochronology of the Hurungwe granite northwest Zimbabwe: Age constraints on the timing of the Magondi orogeny and implications for the correlation between the Kheis and Magondi Belts. *South African Journal of Geology*, *104*(1), 39–46. https://doi.org/10.2113/104.1.39

Miensopust, M. P., Jones, A. G., Muller, M. R., Garcia, X., & Evans, R. L. (2011). Lithospheric structures and Precambrian terrane boundaries in northeastern Botswana revealed through magnetotelluric profiling as part of the Southern African Magnetotelluric Experiment. *Journal of Geophysical Research*, *116*, B02401. https://doi.org/10.1029/2010JB007740

Mulibo, G. D., & Nyblade, A. A. (2013a). The *P* and *S* wave velocity structure of the mantle beneath eastern Africa and the African superplume anomaly. *Geochemistry, Geophysics, Geosystems*, *14*(8), 2696–2715. https://doi.org/10.1002/ggge.20150

Mulibo, G. D., & Nyblade, A. A. (2013b). Mantle transition zone thinning beneath eastern Africa: Evidence for a whole-mantle superplume structure. *Geophysical Research Letters*, *40*(14), 3562–3566. https://doi.org/10.1002/grl.50694

Muller, M. R., Jones, A. G., Evans, R. L., Grütter, H. S., Hatton, C., Garcia, X., et al. (2009). Lithospheric structure, evolution and diamond prospectivity of the Rehoboth Terrane and western Kaapvaal Craton, southern Africa: Constraints from broadband magnetotellurics. *Lithos*, *112*, 93–105. https://doi.org/10.1016/j.lithos.2009.06.023

Nair, S. K., Gao, S. S., Liu, K. H., & Silver, P. G. (2006). Southern African crustal evolution and composition: Constraints from receiver function studies. *Journal of Geophysical Research*, *111*, B02304. https://doi.org/10.1029/2005JB003802

Nguuri, T. K., Gore, J., James, D. E., Webb, S. J., Wright, C., Zengeni, T. G., et al. (2001). Crustal structure beneath southern Africa and its implications for the formation and evolution of the Kaapvaal and Zimbabwe cratons. *Geophysical Research Letters*, *28*(13), 2501–2504. https://doi.org/10.1029/2000GL012587

Nyblade, A. A., & Robinson, S. W. (1994). The African superswell. *Geophysical Research Letters*, *21*(9), 765–768. https://doi.org/10.1029/94GL00631

Nyblade, A. A., & Sleep, N. H. (2003). Long lasting epeirogenic uplift from mantle plumes and the origin of the Southern African Plateau. *Geochemistry, Geophysics, Geosystems*, *4*(12), 1105. https://doi.org/10.1029/2003GC000573

O'Donnell, J. P., Adams, A., Nyblade, A. A., Mulibo, G. D., & Tugume, F. (2013). The uppermost mantle shear wave velocity structure of eastern Africa from Rayleigh wave tomography: Constraints on rift evolution. *Geophysical Journal International*, *194*(2), 961–978. https://doi.org/10.1093/gji/ggt135

Olsson, J. R., Söderlund, U., Klausen, M. B., & Ernst, R. E. (2010). U–Pb baddeleyite ages linking major Archean dyke swarms to volcanic-rift forming events in the Kaapvaal craton (South Africa), and a precise age for the Bushveld Complex. *Precambrian Research*, *183*(3), 490–500. https://doi.org/10.1016/j.precamres.2010.07.009

Ortiz, K., Nyblade, A., van der Meijde, M., Paulssen, H., Kwadiba, M., Ntibinyane, O., et al. (2019). Upper mantle *P*-and *S*-wave velocity structure of the Kalahari Craton and surrounding Proterozoic terranes, southern Africa. *Geophysical Research Letters*, *46*, 9509–9518. https://doi.org/10.1029/2019GL084053

Pasyanos, M. E., & Nyblade, A. A. (2007). A top to bottom lithospheric study of Africa and Arabia. *Tectonophysics*, *444*(1–4), 27–44. https://doi.org/10.1016/j.tecto.2007.07.008

Priestley, K., McKenzie, D., Debayle, E., & Pilidou, S. (2008). The African upper mantle and its relationship to tectonics and surface geology. *Geophysical Journal International*, *175*(3), 1108–1126. https://doi.org/10.1111/j.1365-246X.2008.03951.x

Raveloson, A., Nyblade, A., Fishwick, S., Mangongolo, A., & Master, S. (2015). The upper mantle seismic velocity structure of south-central Africa and the seismic architecture of Precambrian lithosphere beneath the Congo Basin. In *Geology and Resource Potential of the Congo Basin* (pp. 3–18). Berlin, Heidelberg: Springer.

Ritsema, J., & van Heijst, H. (2000). New seismic model of the upper mantle beneath Africa. *Geology*, *28*(1), 63–66. https://doi.org/10.1130/0091-7613(2000)28<63:NSMOTU>2.0.CO;2

Sarafian, E., Evans, R. L., Abdelsalam, M. G., Atekwana, E., Elsenbeck, J., Jones, A. G., & Chikambwe, E. (2018). Imaging Precambrian lithospheric structure in Zambia using electromagnetic methods. *Gondwana Research*, *54*, 38–49. https://doi.org/10.1016/j.gr.2017.09.007

Scholz, C. H., Koczynski, T. A., & Hutchins, D. G. (1976). Evidence for incipient rifting in southern Africa. *Geophysical Journal International*, *44*(1), 135–144. https://doi.org/10.1111/j.1365-246X.1976.tb00278.x

Schutt, D. L., & Lesher, C. E. (2010). Compositional trends among Kaapvaal Craton garnet peridotite xenoliths and their effects on seismic velocity and density. *Earth and Planetary Science Letters*, *300*(3–4), 367–373. https://doi.org/10.1016/j.epsl.2010.10.018

Sebai, A., Stutzmann, E., Montagner, J. P., Sicilia, D., & Beucler, E. (2006). Anisotropic structure of the African upper mantle from Rayleigh and Love wave tomography. *Physics of the Earth and Planetary Interiors*, *155*(1–2), 48–62. https://doi.org/10.1016/j.pepi.2005.09.009

Tugume, F., Nyblade, A., Julià, J., & van der Meijde, M. (2013). Precambrian crustal structure in Africa and Arabia: Evidence lacking for secular variation. *Tectonophysics*, *609*, 250–266. https://doi.org/10.1016/j.tecto.2013.04.027

Van Schijndel, V., Cornell, D. H., Hoffmann, K. H., & Frei, D. (2011). Three episodes of crustal development in the Rehoboth Province, Namibia. *Geological Society, London, Special Publications*, *357*(1), 27–47. https://doi.org/10.1144/SP357.3

VanDecar, J. C. (1991). *Upper-mantle structure of the Cascadia subduction zone from non-linear teleseismic travel-time inversion (Doctoral dissertation)*. Seattle: The University of Washington.

VanDecar, J. C., & Crosson, R. S. (1990). Determination of teleseismic relative phase arrival times using multi-channel cross-correlation and least squares. *Bulletin of the Seismological Society of America*, *80*(1), 150–169.

Weatherall, P., Marks, K. M., Jakobsson, M., Schmitt, T., Tani, S., Arndt, J. E., et al. (2015). A new digital bathymetric model of the world's oceans. *Earth and Space Science*, *2*(8), 331–345. https://doi.org/10.1002/2015EA000107

Weeraratne, D. S., Forsyth, D. W., Fischer, K. M., & Nyblade, A. A. (2003). Evidence for an upper mantle plume beneath the Tanzanian craton from Rayleigh wave tomography. *Journal of Geophysical Research*, *108*(B9), 2427. https://doi.org/10.1029/2002JB002273

Wright, C., Kgaswane, E. M., Kwadiba, M. T. O., Simon, R. E., Nguuri, T. K., & McRae-Samuel, R. (2003). South African seismicity, April 1997 to April 1999, and regional variations in the crust and uppermost mantle of the Kaapvaal craton. *Lithos*, *71*(2–4), 369–392. https://doi.org/10.1016/S0024-4937(03)00122-1

Youssof, M., Thybo, H., Artemieva, I. M., & Levander, A. (2015). Upper mantle structure beneath southern African cratons from seismic finite-frequency *P*-and *S*-body wave tomography. *Earth and Planetary Science Letters*, *420*, 174–186. https://doi.org/10.1016/j.epsl.2015.01.034

Yu, Y., Liu, K. H., Huang, Z., Zhao, D., Reed, C. A., Moidaki, M., et al. (2017). Mantle structure beneath the incipient Okavango rift zone in southern Africa. *Geosphere*, *13*(1), 102–111. https://doi.org/10.1130/GES01331.1

Yu, Y., Liu, K. H., Moidaki, M., Reed, C. A., & Gao, S. S. (2015). No thermal anomalies in the mantle transition zone beneath an incipient continental rift: Evidence from the first receiver function study across the Okavango Rift Zone, Botswana. *Geophysical Journal International*, *202*(2), 1407–1418. https://doi.org/10.1093/gji/ggv229

Yuan, X., Heit, B., Brune, S., Steinberger, B., Geissler, W. H., Jokat, W., & Weber, M. (2017). Seismic structure of the lithosphere beneath NW N amibia: Impact of the T ristan da C unha mantle plume. *Geochemistry, Geophysics, Geosystems*, *18*(1), 125–141. https://doi.org/10.1002/2016GC006645